Journal of Electronic Imaging

SPIEDigitalLibrary.org/jei

Sequential application of viscous opening and lower leveling for three-dimensional brain extraction on magnetic resonance imaging T1

Jorge Domingo Mendiola-Santibañez
Martín Gallegos-Duarte
Miguel Octavio Arias-Estrada
Israel Marcos Santillán-Méndez
Juvenal Rodríguez-Reséndiz
Iván Ramón Terol-Villalobos

SPIE

IS&T
imaging.org

Sequential application of viscous opening and lower leveling for three-dimensional brain extraction on magnetic resonance imaging T1

Jorge Domingo Mendiola-Santibañez,[a,d,*] Martín Gallegos-Duarte,[b] Miguel Octavio Arias-Estrada,[c] Israel Marcos Santillán-Méndez,[d] Juvenal Rodríguez-Reséndiz,[d] and Iván Ramón Terol-Villalobos[a]
[a]Centro de Investigación y Desarrollo Tecnológico en Electroquímica, Parque Tecnológico S/N, San Fandila-Pedro Escobedo, CP 76703, Querétaro, México
[b]Universidad Autónoma de Querétaro, Doctorado de la Facultad de Medicina, Clavel 200, Col Prados de la Capilla, CP 76170, Querétaro, México
[c]Instituto Nacional de Astrofísica, Optica y Electrónica, Coordinación de Ciencias Computacionales, Apdo. Postal 51 y 216, Puebla, Pue. 72000, México
[d]Universidad Autónoma de Querétaro, Centro Universitario S/N, División de Investigación y Posgrado de la Facultad de Ingeniería, CP 76010, Querétaro, México

Abstract. A composition of the viscous opening and the lower leveling is introduced to extract brain in magnetic resonance imaging T1. The innovative transformation disconnects chained components and has better control on the reconstruction process of the marker inside of the original image. However, the sequential operator requires setting several parameters, making its application difficult. Due to this situation, a simplification is carried out on it to obtain a more practical method. The proposed morphological transformations were tested with the Internet Brain Segmentation Repository (IBSR) database, which is used as a benchmark among the community. The results are compared using the Jaccard and Dice indices with respect to (i) manual segmentations obtained from the IBSR, (ii) mean indices reported in the current literature, and (iii) segmentations obtained from the Brain Extraction Tool, since this is one of the most popular algorithms used for brain segmentation. The average indices of Jaccard and Dice indicate that the reduced transformation produces similar results to the other methods reported in the literature while the sequential operator presents a better performance. *© The Authors. Published by SPIE under a Creative Commons Attribution 3.0 Unported License. Distribution or reproduction of this work in whole or in part requires full attribution of the original publication, including its DOI.* [DOI: 10.1117/1.JEI.23.3.033010]

Keywords: viscous opening; lower leveling; brain extraction; chained components; three-dimensional morphological segmentation.

Paper 13663 received Nov. 27, 2013; revised manuscript received Apr. 6, 2014; accepted for publication May 9, 2014; published online Jun. 3, 2014.

1 Introduction

The segmentation of the brain is a task commonly developed in neuroimaging laboratories. The difficulty and importance of the skull stripping problem has led to a wide range of proposals being developed to tackle it. Some techniques reported in the literature to solve this issue are, for example, surfacing models,[1] deformable models,[1–3] watershed,[4,5] morphology,[6] atlas-based methods,[7] hybrid techniques,[8,9] fuzzy regions of interest,[10] histogram analysis,[11] active contours,[12,13] multiresolution approach,[14] multiatlas propagation and segmentation (MAPS),[15,16] topological constraints,[17] and others. Some revision papers concerning brain segmentation can be found in Refs. 18–21.

The problem that arises when having many viable techniques is to choose the ones that have the best performance for a particular visualization task. In Refs. 22–24, the authors selected the popular skull-stripping algorithms reported in the literature and carried out a comparison among them. These algorithms include Brain Extraction Tool (BET),[3] 3dIntracranial,[25] Hybrid Watershed Algorithm,[8] Brain Surface Extractor (BSE),[26] and Statistical Parametric Mapping v.2 (SPM2).[27] The two common and popular methods mentioned in Refs. 22–24 are BET and BSE. According to the results presented in Ref. 23, the authors found that BET and BSE produce similar brain extractions if adequate parameters are used in those algorithms. Interesting information about BET is reported in Ref. 28, where the authors found that the BET algorithm's performance is improved after the removal of the neck slices. Due to the popularity of BET, we will compare our results to that algorithm. Two important characteristics of BET are: it is fast and it generates approximated segmentations.

In this paper, a morphological transformation that disconnects chained components is proposed and applied to segment brain from magnetic resonance imaging (MRI) T1. The operator is built as a composition between the viscous opening[29] and the lower leveling[30] and it is implemented in MATLAB R2010a on a 2.5 GHz Intel Core i5 processor with 2 GB RAM memory. To illustrate the performance of our proposals, two brain MRI datasets of 20 and 18 normal subjects,[31] obtained from the Internet Brain Segmentation Repository (IBSR) and developed by the Centre for Morphometric Analysis (CMA) at the Massachusetts General Hospital (http://www.nitrc.org), were processed.

In order to introduce our proposals, Sec. 2 provides a background on some morphological transformations such as opening and closing by reconstruction,[32] viscous opening, and lower leveling. Other approaches on viscous

*Address all correspondence to: Jorge Domingo Mendiola-Santibañez, E-mail: mendijor@uaq.mx

transformations can be found in Refs. 33–36; however, these transformations work differently because they consider structuring elements that change dynamically, while our proposals work with a geodesic approach.[29]

In Sec. 3, a new transformation is built through the composition of the viscous opening and the leveling. Because the composed transformation uses several parameters, a simplification of it is introduced for facilitating its application. Such a reduction results in approximated segmentations and less time is utilized during its execution. It is noteworthy to mention that the two operators employ determinate size parameters deduced from a granulometric analysis.[37]

The experimental results are presented in Sec. 4. In Sec. 4.1, an explanation is given about the parameters involved in the proposed transformations and the performance of each one is illustrated with several pictures.

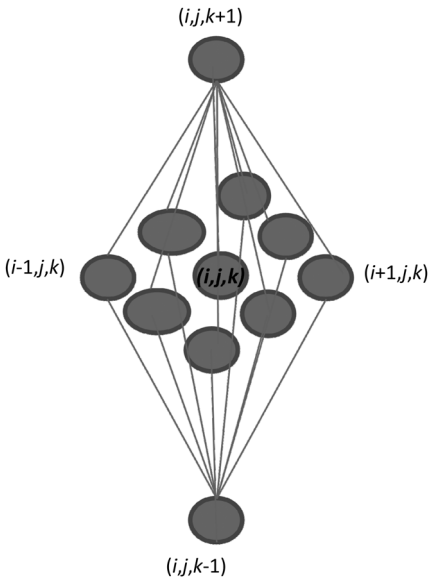

Fig. 1 Three-dimensional (3-D) structuring element used in this paper.

In Sec. 4.2, the results obtained with the morphological transformations are compared using the mean values of the Jaccard[38] and Dice[39] indices with respect to those obtained from: (i) the BET algorithm and (ii) the results reported in Refs. 11, 12, and 40, which utilize the same databases. In Sec. 4.3, the advantages and disadvantages of our method for brain MR image extraction are presented. Section 5 contains our conclusions.

2 Background on Some Morphological Transformations

2.1 *Opening and Closing by Reconstruction*

In mathematical morphology (MM), the basic transformations are the erosion $\varepsilon_{\mu B}(f)(x)$ and dilation $\delta_{\mu B}(f)(x)$, where B represents the three-dimensional (3-D) structuring element which has its origin in the center. Figure 1 illustrates the shape of the structuring element used in this paper. $\check{B}$ denotes the transposed set of B *with* respect its origin, $\check{B} = \{-x: x \in B\}$, μ is a size parameter, $f: Z^3 \to Z$ is the input image, and x is a point on the definition domain.

The next equations represent the morphological erosion $\varepsilon_{\mu B}(f)(x)$ and dilation $\delta_{\mu B}(f)(x)$:[41]

$$\varepsilon_{\mu B}(f)(x) = \wedge \{f(y): y \in \mu\check{B}_x\}$$

and

$$\delta_{\mu B}(f)(x) = \wedge \{f(y): y \in \mu\check{B}_x\},$$

where $\vee$ and $\wedge$ represent the inf and sup operators. The morphological erosion and dilation permit us to build other types of transformations; these include the morphological opening $\gamma_{\mu B}(f)(x)$ and closing $\varphi_{\mu B}(f)(x)$ defined as

$$\gamma_{\mu B}(f)(x) = \delta_{\mu\check{B}}[\varepsilon_{\mu B}(f)](x)$$

and

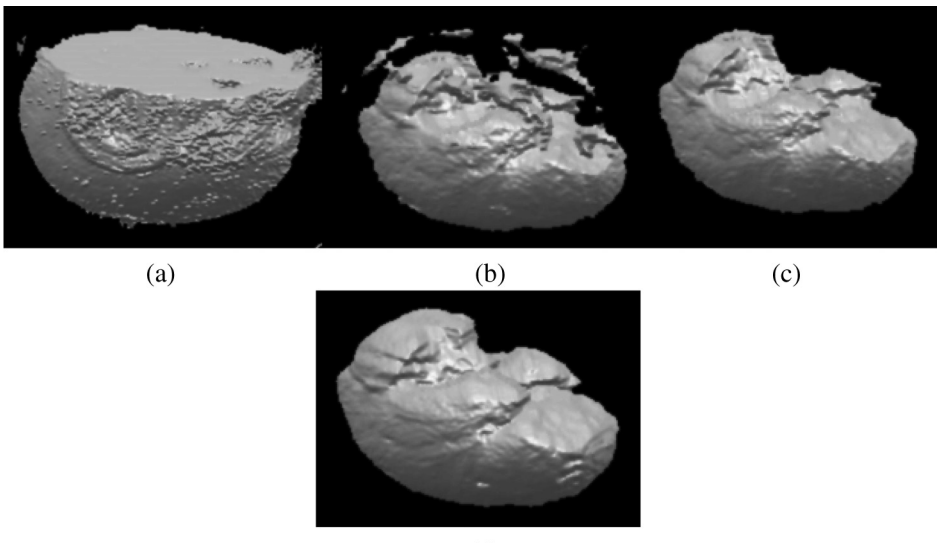

Fig. 2 Viscous opening illustration: (a) original volume f, (b) $\varepsilon_{\lambda=6}(f)$, (c) $\gamma_{\mu=16-\lambda=10}\varepsilon_{\lambda=6}(f)$, and (d) $\delta_{\lambda=6}\,\gamma_{\mu=10}\varepsilon_{\lambda=6}(f)$.

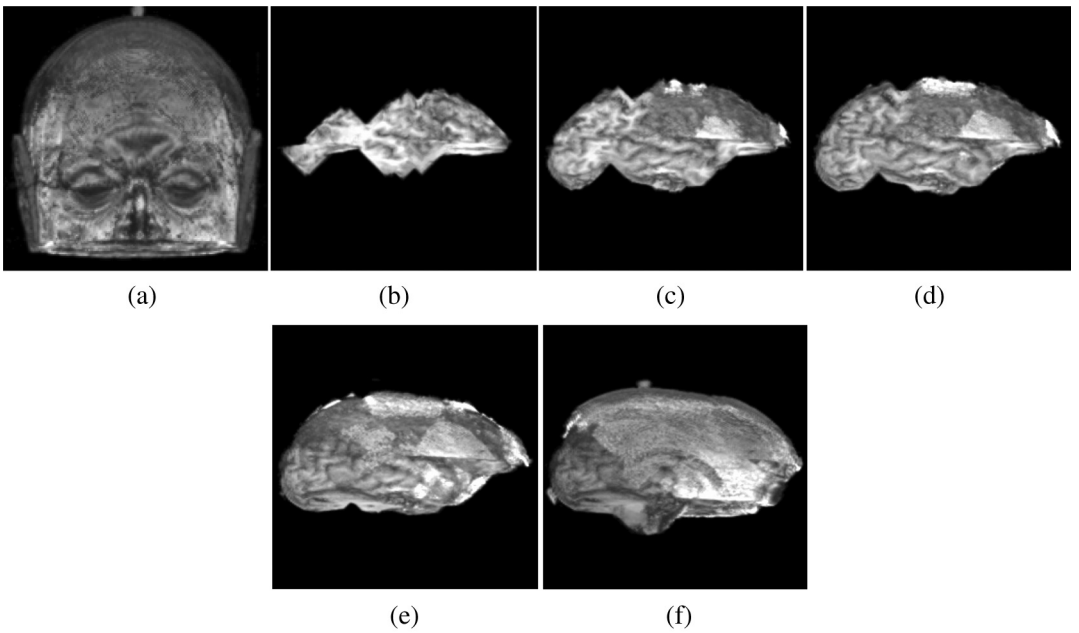

Fig. 3 3-D brain segmentation using Eqs. (5) and (6). (a) Original volume f; (b) marker by opening defined in Eq. (6); (c) result of Eq. (5) using the marker obtained in (b) with $\alpha = 4$; (d) result of Eq. (5) using the marker obtained in (b) with $\alpha = 3$; (e) result of Eq. (5) using the marker obtained in (b) with $\alpha = 2$, and (f) result of Eq. (5) using the marker obtained in (b) with $\alpha = 1$.

$$\varphi_{\mu B}(f)(x) = \varepsilon_{\mu\check{B}}[\delta_{\mu B}(f)](x).$$

In addition, the opening (closing) by reconstruction has the characteristic of modifying the regional maxima (minima) without affecting the remaining components to a large extent. These operators use the geodesic transformations.[32,42] The geodesic dilation $\delta_f^1(g)$ and erosion $\varepsilon_f^1(g)$ are expressed as $\delta_f^1(g) = f \wedge \delta_B(g)$ with $g \leq f$, and $\varepsilon_f^1(g) = f \vee \varepsilon_B(g)$ considering $g \geq f$, respectively. When the function g is equal to the morphological erosion or dilation, the opening $\tilde{\gamma}_{\mu B}(f)(x)$ or closing $\tilde{\varphi}_{\mu B}(f)(x)$ by reconstruction is obtained. Formally, the next expressions represent them

$$\tilde{\gamma}_{\mu B}(f)(x) = \underbrace{\delta_f^1 \delta_f^1 \cdots \delta_f^1[\varepsilon_{\mu B}(f)]}_{\text{until stability}}(x) \tag{1}$$

and

$$\tilde{\varphi}_{\mu B}(f)(x) = \underbrace{\varepsilon_f^1 \varepsilon_f^1 \cdots \varepsilon_f^1[\delta_{\mu B}(f)]}_{\text{until stability}}(x).$$

2.2 *Viscous Opening $\gamma_{\lambda,\mu}$ and Viscous Difference*

The viscous opening $\tilde{\gamma}_{\lambda,\mu}$ and closing $\tilde{\varphi}_{\lambda,\mu}$ defined in Ref. 29 allow one to deal with overlapped or chained components.

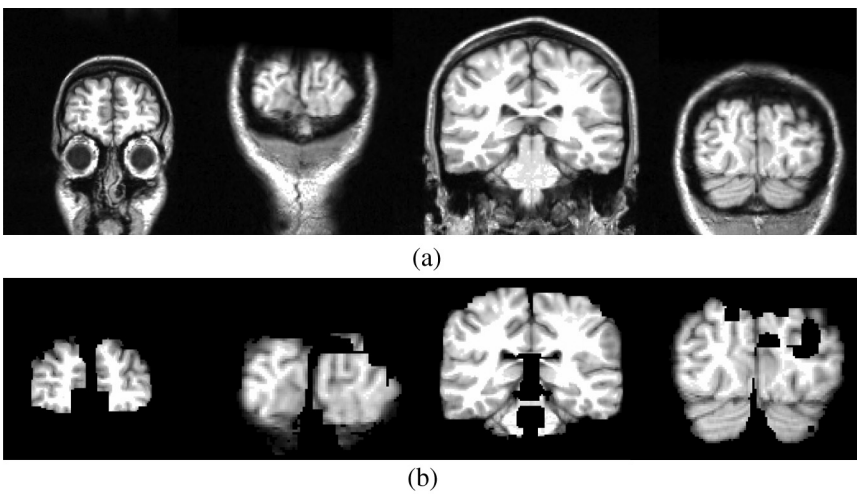

Fig. 4 Segmentation of a volume [taken from the database Internet Brain Segmentation Repository (IBSR) with 20 subjects] using Eq. (7). (a) Slices of the original volume and (b) slices corresponding to $\eta_{\mu=1,\alpha_2=20,\lambda_2=8,\mu_2=10,\alpha_1=10,\lambda_1=10,\mu_1=12}(f)$.

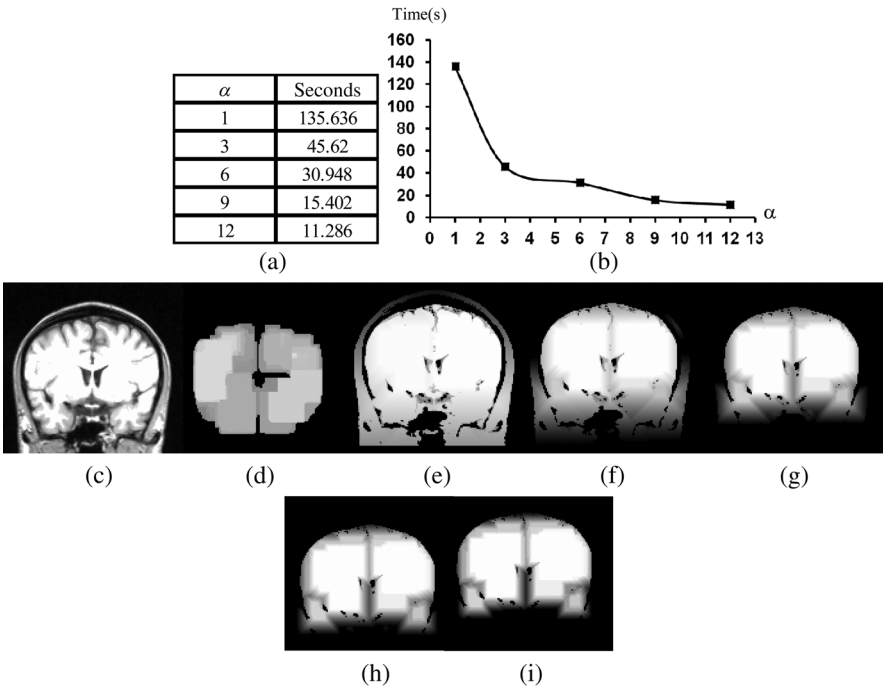

Fig. 5 Execution time of Eq. (5) and some output slices corresponding to several processed volumes. (a) Time spent to compute Eq. (5) considering 60 slices, the marker corresponds to the viscous opening with $\lambda = 10$, $\mu = 12$. The leveling is applied considering $\alpha = 1, 3, 6, 9, 12$; (b) graph corresponding to the data presented in (a); (c) slice of the original volume; (d) brain section taking from the viscous opening and used as marker; (e)–(i) set of slices taken from the volumes processed with $\alpha = 1, 3, 6, 9, 12$, as is illustrated in Fig. 4.

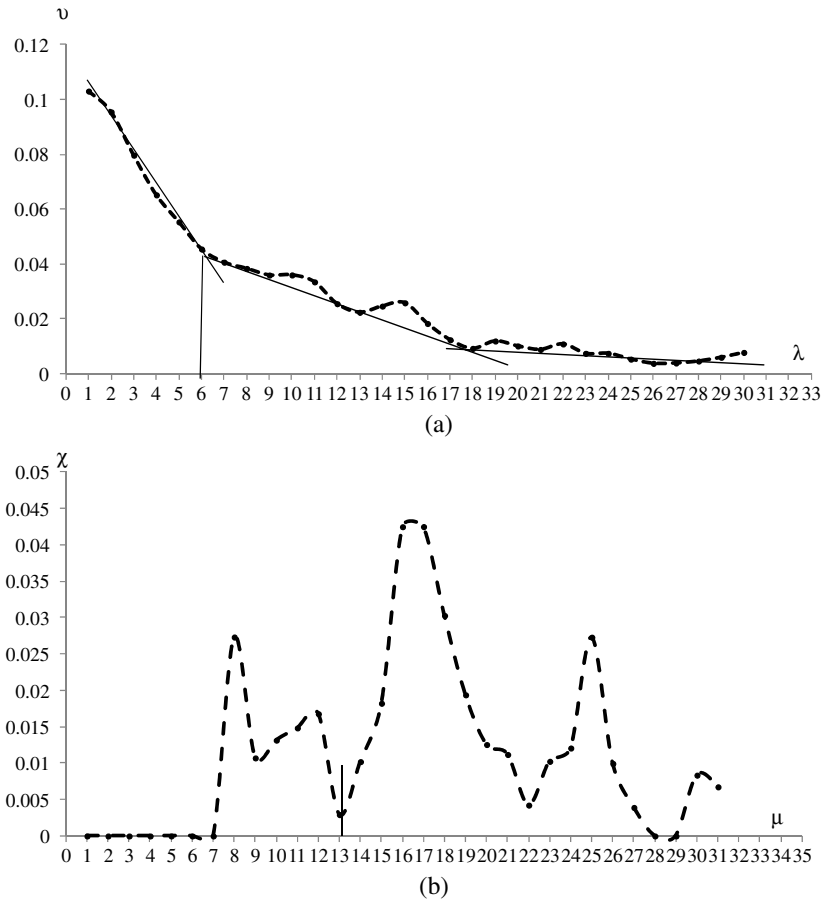

Fig. 6 Granulometric curves computed on certain volume taken from the database IBSR with 20 subjects. (a) Granulometry computed from Eq. (10) and (b) viscous granulometry obtained from Eq. (11).

These transformations are denoted by

$$\tilde{\gamma}_{\lambda,\mu}(f) = \delta_\lambda \tilde{\gamma}_{\mu-\lambda}\varepsilon_\lambda(f) \quad \text{with } \lambda \le \mu \tag{2}$$

and

$$\tilde{\varphi}_{\lambda,\mu}(f) = \varepsilon_\lambda \tilde{\varphi}_{\mu-\lambda}\delta_\lambda(f) \quad \text{with } \lambda \le \mu.$$

Equation (2) uses three operators, the morphological erosion ε_λ, the opening by reconstruction $\tilde{\gamma}_{\mu-\lambda}$, and the morphological dilation δ_λ. The morphological erosion $\varepsilon_\lambda(f)$ allows one to discover and disconnect the λ-components (all components where the structuring element can go from one place to another by a continuous path made of squares and whose centers move along this path). Then, the opening by reconstruction $\tilde{\gamma}_{\mu-\lambda}\varepsilon_\lambda(f)$ removes all regions less than $\mu-\lambda$ around the λ-components. Finally, because the viscous opening is defined on the lattice of dilatation, the δ_λ must be obtained on $\tilde{\gamma}_{\mu-\lambda}\varepsilon_\lambda(f)$. An example of Eq. (2) is given in Fig. 2. The original image is exhibited in Fig. 2(a). Figure 2(b) shows the morphological erosion $\varepsilon_{\lambda=6}(f)$. Notice that there are several components around the brain. The image in Fig. 2(c) corresponds to the transformation $\tilde{\gamma}_{\mu=16-\lambda=10}\varepsilon_{\lambda=6}(f)$. In this image, several components have been eliminated by the process of opening by reconstruction. Figure 2(d) displays the result of the transformation $\delta_{\lambda=6}\ \tilde{\gamma}_{\mu=10}\varepsilon_{\lambda=6}(f)$.

Viscous openings permit the sieving of the image through the viscous difference.[29] This is defined in

$$\tilde{\gamma}_{\lambda,\mu_1}(f) \div \tilde{\gamma}_{\lambda,\mu_2}(f) = \delta_\lambda[\tilde{\gamma}_{\mu_1-\lambda}(\varepsilon_\lambda) - \tilde{\gamma}_{\mu_2-\lambda}(\varepsilon_\lambda)] \quad \text{with } \lambda \le \mu_1 \le \mu_2. \tag{3}$$

According to the explanation given above, the erosion ε_λ discovers the λ-components and the difference $\tilde{\gamma}_{\mu_1-\lambda}(\varepsilon_\lambda) - \tilde{\gamma}_{\mu_2-\lambda}(\varepsilon_\lambda)$ with $\lambda \le \mu_1 \le \mu_2$ sieving the image, whereas δ_λ is necessary to obtain the viscous component. The viscous difference gives the information of all discovered disconnected components of a certain size λ when μ is increased.

Table 1 Parameters corresponding to Eq. (9). The processed dataset was IBSR1.

Volume	λ_1	μ_1	ρ_1	a_1	μ	α_1	ρ_2	a_2	λ_2	μ_2	ρ_3	a_3	μ	α_2	ρ_4	a_4
IBSR1_001	8	10	3	90	1	8	5	60	5	8	5	100	1	30	8	100
IBSR1_002	8	10	3	90	1	8	5	60	5	8	5	100	1	20	8	80
IBSR1_004	8	10	8	30	1	7	8	10	5	10	10	60	1	120	8	30
IBSR1_005	12	13	3	10	1	18	3	50	10	12	3	50	1	45	5	30
IBSR1_006	10	12	4	50	1	25	4	50	12	13	5	60	1	20	5	60
IBSR1_007	10	12	8	10	1	10	8	50	8	10	8	50	1	60	5	100
IBSR1_008	10	12	8	10	1	11	8	90	8	10	8	50	1	40	5	100
IBSR1_011	12	14	5	20	1	15	5	20	10	12	5	100	1	25	8	40
IBSR1_012	11	12	4	50	1	30	4	70	11	12	5	100	1	22	5	120
IBSR1_013	12	14	5	20	1	15	5	90	8	9	12	100	1	35	12	120
IBSR1_015	10	14	8	1	1	12	8	1	8	9	12	40	1	20	12	80
IBSR1_016	8	10	3	20	1	12	5	60	5	8	5	60	1	40	8	110
IBSR1_017	8	10	3	20	1	12	5	60	6	8	5	60	1	40	8	110
IBSR1_100	12	14	3	90	1	8	5	60	5	8	5	100	1	30	8	100
IBSR1_110	10	12	3	90	1	20	5	60	5	8	5	100	1	100	8	100
IBSR1_111	12	14	3	90	1	8	5	60	5	8	5	100	1	30	8	100
IBSR1_112	10	12	3	90	1	20	5	60	5	8	5	100	1	12	8	100
IBSR1_191	10	12	3	90	1	20	5	60	5	8	5	100	1	20	8	100
IBSR1_202	12	14	3	90	1	8	5	60	5	8	5	100	1	30	8	100
IBSR1_205	10	12	3	90	1	20	5	60	5	8	5	100	1	20	8	100

2.3 *Lower Leveling*

The lower leveling transformation is presented as follows:[30]

$$\psi^1_{\mu,\alpha}(f,g) = f \wedge \{g \vee [\delta_\mu(g) - \alpha]\}, \tag{4}$$

where f is the reference image, g is a marker, $\alpha \in [0,255]$ is a positive scalar called slope, and μ is the size of the structuring element. Equation (4) is iterated until stability is reached with the purpose of reconstructing the marker g at the interior of the original mask f, i.e.,

$$\Psi^\infty_{\mu,\alpha}(f,g) = \lim_{n\to\infty} \psi^n_{\mu,\alpha}(f,g) = \underbrace{\psi^1_{\mu,\alpha} \cdots \psi^1_{\mu,\alpha}[\psi^1_{\mu,\alpha}(g)]}_{\text{until stability}}. \tag{5}$$

On the other hand, the selection of the marker g is very important. In Ref. 30, for example, the following marker was used to segment the brain:

$$\mathrm{g} = \gamma_{\mu B}(f). \tag{6}$$

The parameter α helps to control the reconstruction of the marker g into f. An example to illustrate the performance of Eq. (5) is given in the next section.

3 Segmentation of Brain in MRI T1

Equations (2), (5), and (6) were applied in Refs. 29 and 30 to separate the skull and the brain on slices of an MRI T1 for the two-dimensional (2-D) case. These transformations allow disconnecting overlapped components, because they can control the reconstruction process. In 2-D, the structuring element moves and uniquely touches one image. However, for the 3-D case, neighbors within the structuring element are taken from three adjacent brain slices. Due to this, several regions are connected through the shape of the 3-D structuring element among the different brain sections, resulting in, as a consequence, a major connectivity. The increase in connectivity originates that Eqs. (2) and (5) for the 3-D case do not show the same performance as in the 2-D case, and the component of the brain cannot be separated by applying such operators once.

This situation is illustrated in Fig. 3 where Eq. (5) has been applied considering the marker obtained by Eq. (6). The original volume appears in Fig. 3(a). Figure 3(b) displays a portion of the brain obtained from Eq. (6) with $\mu = 25$. The set of images in Figs. 3(c)–3(f) illustrates the control in the reconstruction process using different slopes α. However, the extracted brain contains additional components since this condition is inadequate. The next section provides a solution to this problem.

3.1 *Composition of Morphological Connected Transformations*

As previously stated, viscous opening and lower leveling allow separating the chained components, and it is natural to think of combining both operators to get one transformation capable of having better control on the reconstruction process. Following this idea, an option is to use the viscous opening as a marker of the lower leveling to eliminate a great portion of the skull; posteriorly, the resulting image is again processed with a similar filter to eliminate the remaining regions around the brain. Such a procedure represents a sequential application of the combined transformations considering different parameters in order to have increasing control in the reconstruction process. The purpose is to eliminate the skull softly in two steps. The following equation permits the disconnection of the chained components and comes from the combination of Eqs. (2) and (5):

$$\eta_{\mu,\alpha_2,\lambda_2,\mu_2,\alpha_1,\lambda_1,\mu_1}(f)(x) = \Psi^\infty_{\mu,\alpha_2}(f, \tilde{\gamma}_{\lambda_2,\mu_2}\{\Psi^\infty_{\mu,\alpha_1}[f, \tilde{\gamma}_{\lambda_1,\mu_1}(f)]\})(x). \tag{7}$$

Nevertheless, Eq. (7) produces an unsatisfactory performance. Figure 4 shows an example of the transformation $\eta_{\mu=1,\alpha_2=20,\lambda_2=8,\mu_2=10,\alpha_1=10,\lambda_1=10,\mu_1=12}(f)$. Some slices of the original volume can be seen in Fig. 4(a) where the segmentation results in the creation of holes on the brain, as is illustrated in Fig. 4(b). The viscous opening causes this behavior, since all components not supporting the morphological erosion of size λ will merge with the background because the 3-D structuring element produces stronger changes as

Table 2 Parameters corresponding to Eq. (12). The processed dataset was IBSR1.

Volume	λ_1	μ_1	ρ_1	a_1	μ	α_1	ρ_2	a_2
IBSR1_001	10	12	4	52	1	14	5	54
IBSR1_002	11	13	5	53	1	15	6	55
IBSR1_004	11	13	5	50	1	8	6	20
IBSR1_005	8	10	5	10	1	7	6	15
IBSR1_006	10	12	4	10	1	10	5	10
IBSR1_007	10	12	4	52	1	14	5	54
IBSR1_008	10	12	4	52	1	14	5	54
IBSR1_011	10	12	4	52	1	14	5	54
IBSR1_012	10	12	4	52	1	14	5	54
IBSR1_013	10	12	4	52	1	14	5	70
IBSR1_015	10	12	4	1	1	3	5	1
IBSR1_016	10	12	4	52	1	14	5	54
IBSR1_017	10	12	4	52	1	14	5	54
IBSR1_100	10	12	4	52	1	14	5	54
IBSR1_110	10	12	4	52	1	14	5	90
IBSR1_111	10	12	4	52	1	14	5	54
IBSR1_112	10	12	4	52	1	14	5	54
IBSR1_191	10	12	4	52	1	14	5	54
IBSR1_202	10	12	4	52	1	14	5	54
IBSR1_205	10	12	4	52	1	14	5	54

the size of the structuring element is increased. One way to get better segmentations consists of computing the operator in Eq. (8), where f is the input image, $\bar{h}_\rho$ represents the mean filter of size ρ, and T_a expresses a threshold between $[a, 255]$ sections. The mean filter $\bar{h}_\rho$ partially closes the holes, T_a and permits the selection of certain regions of interest, and $\xi_{\rho,a}$ helps to obtain a portion of the original image

$$\xi_{\rho,a}(f) = f \wedge T_a \bar{h}_\rho(f). \tag{8}$$

The combination of Eqs. (7) and (8) gives the next operator as a result

$$\eta^*_{\rho_4,a_4,\alpha_2,\rho_3,a_3,\lambda_2,\mu_2,\rho_2,a_2,\mu,\alpha_1,\rho_1,a_1,\lambda_1,\mu_1}(f)(x) = \xi_{\rho_4,a_4}\Psi^\infty_{\mu,\alpha_2}(f, \xi_{\rho_3,a_3}\tilde{\gamma}_{\lambda_2,\mu_2}\{\xi_{\rho_2,a_2}\Psi^\infty_{\mu,\alpha_1}[f, \xi_{\rho_1,a_1}\tilde{\gamma}_{\lambda_1,\mu_1}(f)]\})(x). \tag{9}$$

To apply Eq. (9), the reasoning below needs to be considered.

3.2 *Parameters α, λ, and μ*

3.2.1 *Parameter α*

The following analysis corresponds to Eq. (5) since Eq. (9) uses it. Large α values produce (i) a time reduction in reaching the final result and (ii) a larger control in the reconstruction process.

The quantification of the time when Eq. (5) is applied on a volume of 60 slides—using as a marker $\tilde{\gamma}_{\lambda=10,\mu=12}$ and the lower leveling $\Psi^\infty_{\mu=1,\alpha}$ with $\alpha = 1, 3, 6, 9, 12$—is presented in Fig. 5. This figure displays several slices belonging to the output volumes obtained for different α values.

3.2.2 *Parameter λ*

The adequate election of the parameter λ will bring, as a consequence, the disconnection between the skull and the brain. Such a parameter is computed from a granulometric analysis applying Eq. (10)[37]

$$\upsilon = \frac{\mathrm{vol}[\gamma_\lambda(f)] - \mathrm{vol}[\gamma_{\lambda+1}(f)]}{\mathrm{vol}[f]}, \tag{10}$$

Table 3 Parameters corresponding to Eq. (9). The processed dataset was IBSR2.

Volume	λ_1	μ_1	ρ_1	a_1	μ	α_1	ρ_2	a_2	λ_2	μ_2	ρ_3	a_3	μ	α_2	ρ_4	a_4
IBSR2_001	10	12	4	52	1	14	5	54	6	9	6	81	1	37	7	89
IBSR2_002	10	12	4	52	1	14	5	54	6	9	6	81	1	37	7	89
IBSR2_003	14	15	4	20	1	20	5	20	5	6	6	40	1	40	6	40
IBSR2_004	10	12	4	52	1	10	5	50	5	6	6	20	1	30	6	40
IBSR2_005	10	12	4	52	1	10	5	50	10	12	6	40	1	80	6	40
IBSR2_006	10	12	4	52	1	10	5	50	5	6	6	20	1	20	6	50
IBSR2_007	8	10	5	20	1	10	5	10	8	10	8	30	1	20	4	20
IBSR2_008	11	12	4	50	1	2	5	60	6	10	4	50	1	12	6	10
IBSR2_009	11	12	4	50	1	3	5	80	6	8	6	80	1	10	6	80
IBSR2_010	17	18	4	20	1	3	5	50	10	12	6	50	1	1	6	50
IBSR2_011	12	13	4	50	1	8	5	80	8	10	6	80	1	5	6	80
IBSR2_012	11	12	4	50	1	3	5	80	6	8	6	80	1	6	6	60
IBSR2_013	11	12	4	50	1	3	5	80	6	8	6	80	1	10	6	80
IBSR2_014	11	12	4	50	1	3	5	80	6	8	6	80	1	10	6	80
IBSR2_015	11	12	4	50	1	3	5	80	8	10	6	80	1	40	6	80
IBSR2_016	11	12	4	50	1	3	5	80	10	12	6	80	1	25	6	80
IBSR2_017	11	12	4	50	1	3	5	80	10	12	6	80	1	30	6	80
IBSR2_018	11	12	4	50	1	3	5	80	10	12	6	40	1	15	6	20

Table 4 Parameters corresponding to Eq. (12). The processed dataset was IBSR2.

Volume	λ_1	μ_1	ρ_1	a_1	μ	α_1	ρ_2	a_2
IBSR2_001	10	12	4	52	1	14	5	54
IBSR2_002	10	12	4	52	1	14	5	54
IBSR2_003	10	12	4	52	1	8	5	30
IBSR2_004	10	12	4	52	1	14	5	54
IBSR2_005	14	16	4	52	1	16	5	80
IBSR2_006	10	12	4	52	1	14	5	54
IBSR2_007	10	12	4	52	1	4	5	20
IBSR2_008	8	12	4	50	1	4	5	10
IBSR2_009	10	12	4	20	1	5	5	40
IBSR2_010	6	8	4	10	1	2	5	40
IBSR2_011	8	12	4	90	1	4	5	80
IBSR2_012	12	13	4	50	1	4	5	60
IBSR2_013	10	12	4	52	1	14	5	54
IBSR2_014	10	12	4	52	1	14	5	54
IBSR2_015	10	12	4	52	1	17	5	54
IBSR2_016	10	12	4	52	1	18	5	54
IBSR2_017	10	12	4	52	1	14	5	54
IBSR2_018	10	12	4	52	1	5	5	30

where vol stands for the volume, i.e., the sum of all gray levels in the image, and $\gamma_\lambda(f)$ represents the morphological opening size λ. The graph in Fig. 6(a) corresponds to the application of Eq. (10) taking $\lambda \in [1, 30]$. This graph has three important intervals. The interval where $\lambda \in [1, 6]$ shows the elimination of an important part of the skull. Hence, in order to detect the brain, λ will take values greater than 6, i.e., $\lambda \geq 6$.

3.2.3 *Parameter μ*

The parameter μ will be computed using the viscous granulometry χ which is the term of the viscous difference defined in Eq. (3)[29]

$$\chi = \frac{\mathrm{vol}[\tilde{\gamma}_{\lambda,\mu_1}(f) \div \tilde{\gamma}_{\lambda,\mu_2}(f)]}{\mathrm{vol}(f)}. \tag{11}$$

To apply Eq. (11), the next parameters will be considered: $\mu_1, \mu_2 \in [1, 30]$, and $\lambda = 7$ (from the previous analysis for λ), in order to detect the brain component.

Figure 6(b) displays the graph of Eq. (11). For $\mu \in [7, 13]$, the brain component is detected.

3.3 *Simplification of Eq. (9)*

The fact of sequentially applying two transformations along with a mask to obtain Eq. (9) brings as a consequence the use of a large number of parameters. This problem is considered and a simplification is proposed as follows:

$$\tau_{\mu,\rho_1,a_1,\lambda_1,\mu_1}(f)(x) = \Psi^{\infty}_{\mu,\alpha_1}[f, \xi_{\rho_1,a_1}\tilde{\gamma}_{\lambda_1,\mu_1}(f)](x). \tag{12}$$

According to Eq. (12), the marker $\xi_{\rho_1,a_1}\tilde{\gamma}_{\lambda_1,\mu_1}$ is obtained from the viscous opening, and it is propagated by the lower leveling transformation $\Psi^{\infty}_{\mu,\alpha_1}$. Equation (12) presents the following benefits when compared with respect to Eq. (9): (1) the use of fewer parameters and (2) a reduction of the

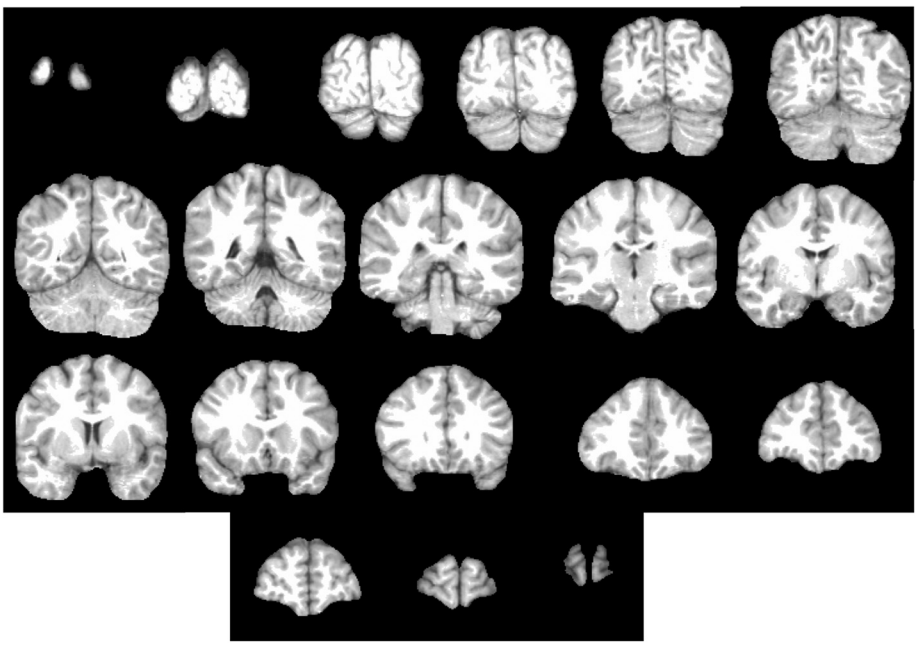

Fig. 7 Some brain slices corresponding to the segmentation of the volume IBSR1_100 using Eq. (9) with the parameters defined in Table 1.

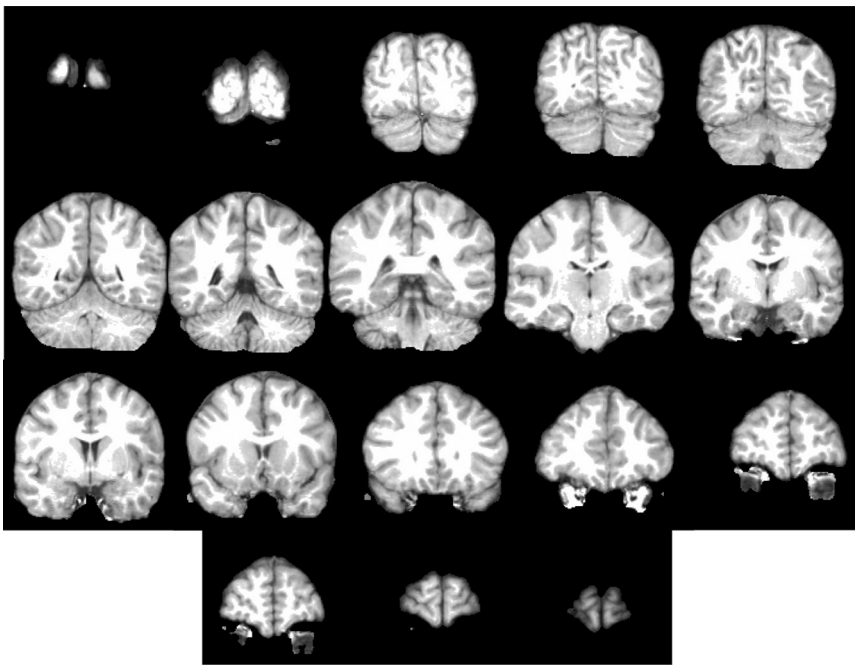

Fig. 8 Some brain slices corresponding to the segmentation of the volume IBSR1_100 using Eq. (12) with the parameters defined in Table 2.

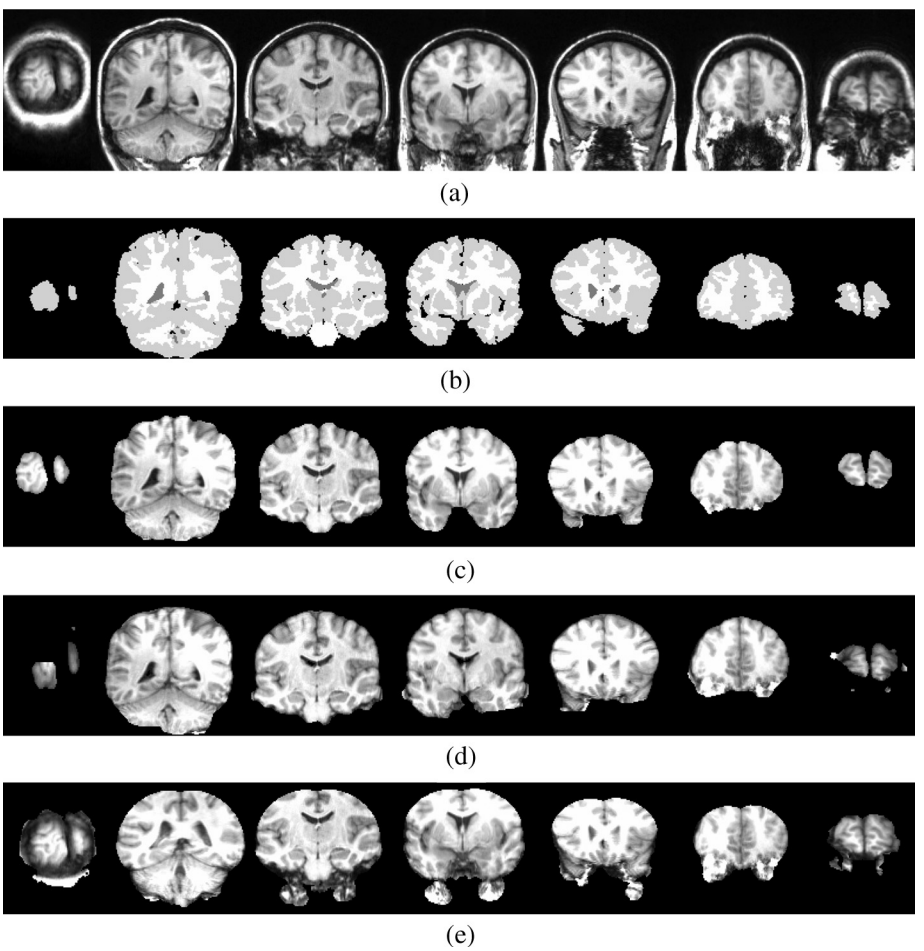

Fig. 9 Images illustrating the segmentation of volume IBSR1_016 through several methods. (a) Brain sections corresponding to the original volume IBSR1_016; (b) manual segmentations provided by the IBSR website; (c) application of Eq. (9) with the parameters defined in Table 1; (d) application of Eq. (12) with the parameters defined in Table 2; and (e) slices obtained from BET using a fractional intensity = 0.5 and vertical gradient = 0.0.

execution time. The performances of Eqs. (9) and (12) are illustrated in Sec. 4.

4 Experimental Results

For the purpose of measuring the performance of our proposed method, the following MRI databases taken from the IBSR and developed by the CMA at the Massachusetts General Hospital (http://www.nitrc.org)[31] are utilized: (i) 20 simulated T1W MRI images (denoted as IBSR1) and (ii) 18 real T1W MRI images (denoted as IBSR2), with a slice thickness of 1.5 mm.

4.1 *Parameters Involved in Eqs. (9) and (12)*

Tables 1–4 contain the parameters used in Eqs. (9) and (12) to segment the volumes belonging to the IBSR1 and IBSR2 datasets. In the volumes of IBSR1, the neck was cropped to obtain similar images to those of IBSR2. Differences among the volumes with respect to the intensity, size, and connectivity, originate the parameters' variation. The guidelines for the parameter selection are given below:

Analysis for Eq. (9):

i. Parameters λ_1, μ_1, λ_2, and μ_2 take their values into the interval [8, 14]. Furthermore, those volumes complying with $\lambda_1 \geq \lambda_2$ and $\mu_1 \geq \mu_2 \geq \lambda_1 \geq \lambda_2$ fulfill the order relation $\tilde{\gamma}_{\lambda_1,\mu_1} \leq \tilde{\gamma}_{\lambda_2,\mu_2}$.

ii. The parameter ρ takes its values within the interval [3, 12]. The mean filter will partially close several holes produced by the viscous opening as those presented in Fig. 4(b). Into MM, the closing transformation fills holes; however, from Fig. 4(b), the background and the holes represent the same region. This means that larger sizes of the structuring element will close the holes; nevertheless, this practice will increase the execution time of Eq. (9).

iii. The parameter a represents a threshold. This varies in the interval [1, 120]. The application of a threshold obeys two things: (a) it eliminates some of the undesirable dark components such as dura matter, skin, and fat and (b) it obtains an appropriated marker.

iv. The lower leveling defined in Eq. (4) and utilized in Eq. (5) uses the parameters μ and α. The size $\mu = 1$ of the morphological dilation keeps its value during the processing with the purpose of detecting the different structures of the brain closer to the input image, whereas the slope α varies in the interval [7, 120]. When parameter α increases, a finer control is obtained, i.e., a smooth transition is generated in each iteration. Figure 7 shows an example of Eq. (9), considering the information of Table 1.

Analysis for Eq. (12):

v. The intervals defined previously are valid for Eq. (12). However, notice that the viscous opening and the lower leveling are applied once. For this situation, the viscous opening must get an appropriated marker containing the brain, and the lower leveling will reconstruct this marker inside the original volume. The transition (dura mater) between the skull and the brain avoids the lower leveling reconstructing the skull completely. Figure 8 displays an example of Eq. (12) by considering the information of Table 2. The input volume used to exemplify Eq. (12) was the same as that used in Fig. 7.

4.2 *Comparison Results*

Figure 9 illustrates the resulting segmentation corresponding to the volume IBSR1_16 under the application of Eqs. (9), (12), and by BET (default parameters) implemented in the MRIcro software.[43] Figure 9(a) shows the original slices. Figure 9(b) displays the respective manual segmentations.

Table 5 Jaccard and Dice indexes corresponding to IBSR1 dataset and segmented with BET, Eqs. (9) and (12) considering the parameters presented in Tables 1 and 2.

	BET		Eq. (12)		Eq. (9)	
Volume	Jaccard	Dice	Jaccard	Dice	Jaccard	Dice
IBSR1_001	0.7949	0.8857	0.9031	0.9491	0.9538	0.9763
IBSR1_002	0.9091	0.9524	0.9267	0.9620	0.9431	0.9707
IBSR1_004	0.8539	0.9212	0.8318	0.9082	0.9482	0.9734
IBSR1_005	0.4721	0.6414	0.7281	0.8427	0.8817	0.9372
IBSR1_006	0.5335	0.6958	0.7981	0.8877	0.8948	0.9445
IBSR1_007	0.8790	0.9356	0.9441	0.9713	0.9586	0.9789
IBSR1_008	0.7587	0.8628	0.9359	0.9669	0.9458	0.9722
IBSR1_011	0.8444	0.9157	0.8972	0.9458	0.9233	0.9601
IBSR1_012	0.8130	0.8968	0.8800	0.9362	0.9018	0.9484
IBSR1_013	0.8873	0.9403	0.8822	0.9374	0.8855	0.9392
IBSR1_015	0.3976	0.5690	0.7070	0.8284	0.9252	0.9612
IBSR1_016	0.6575	0.7933	0.9115	0.9537	0.9526	0.9757
IBSR1_017	0.6730	0.8045	0.9182	0.9573	0.9556	0.9773
IBSR1_100	0.9085	0.9520	0.9337	0.9657	0.9617	0.9805
IBSR1_110	0.9085	0.9520	0.9160	0.9562	0.9395	0.9688
IBSR_111	0.8233	0.9031	0.8954	0.9448	0.9354	0.9666
IBSR_112	0.8347	0.9099	0.9151	0.9557	0.9346	0.9662
IBSR_191	0.9243	0.9607	0.9406	0.9694	0.9601	0.9797
IBSR_202	0.9082	0.9519	0.9324	0.9650	0.9593	0.9792
IBSR_205	0.9085	0.9520	0.9347	0.9663	0.9547	0.9768

Figure 9(c) presents the application of Eq. (9) with the parameters given in Table 1. Figure 9(d) presents the application of Eq. (12) with the parameters given in Table 2. Figure 9(e) shows the brain extraction using the BET algorithm. The parameters selected for the set of 20 brains are intensity threshold = 0.50 and vertical gradient = 0.0. In order to compare the segmentations, the Jaccard and the Dice coefficients are computed. Table 5 contains the indices corresponding to BET and Eqs. (12) and (9) for the IBSR1.

A similar procedure is applied to the IBSR2 database. Figure 10 presents the segmentations corresponding to the IBSR2_04 volume. Figure 10(a) shows the original slices. Figure 10(b) displays the respective manual segmentations. Figure 10(c) presents the application of Eq. (9) with the parameters given in Table 3. Figure 9(d) presents the application of Eq. (12) with the parameters given in Table 4. Figure 9(e) shows the brain extraction using the BET algorithm with the default parameters. Table 6 contains the Jaccard and Dice indices corresponding to BET and Eqs. (12) and (9) for the IBSR2.

Table 7 contains the mean values of the indices presented in Tables 5 and 6 together with the mean values of the indices reported in Refs. 11, 12, and 40.

4.3 *Discussion*

Some commentaries on the segmented volumes are presented as follows:

i. The time performance of our operators is slow compared to the BET algorithm. The table in Fig. 11(a) presents several times measured during the execution of Eq. (9) and considering an increasing numbers of slices. Its corresponding graph is shown in Fig. 9(b). A similar behavior is presented using Eq. (12), but within half the time.

   For the processing of 60 brain slices utilizing Eq. (9), our method spent 354.8 s [177.4 s using Eq. (12)], while the BET algorithm required 8 s.

   In Ref. 24, the measured time to separate brain components varies between 40 s (BET algorithm) to 35 min (SPM2) when considering a complete

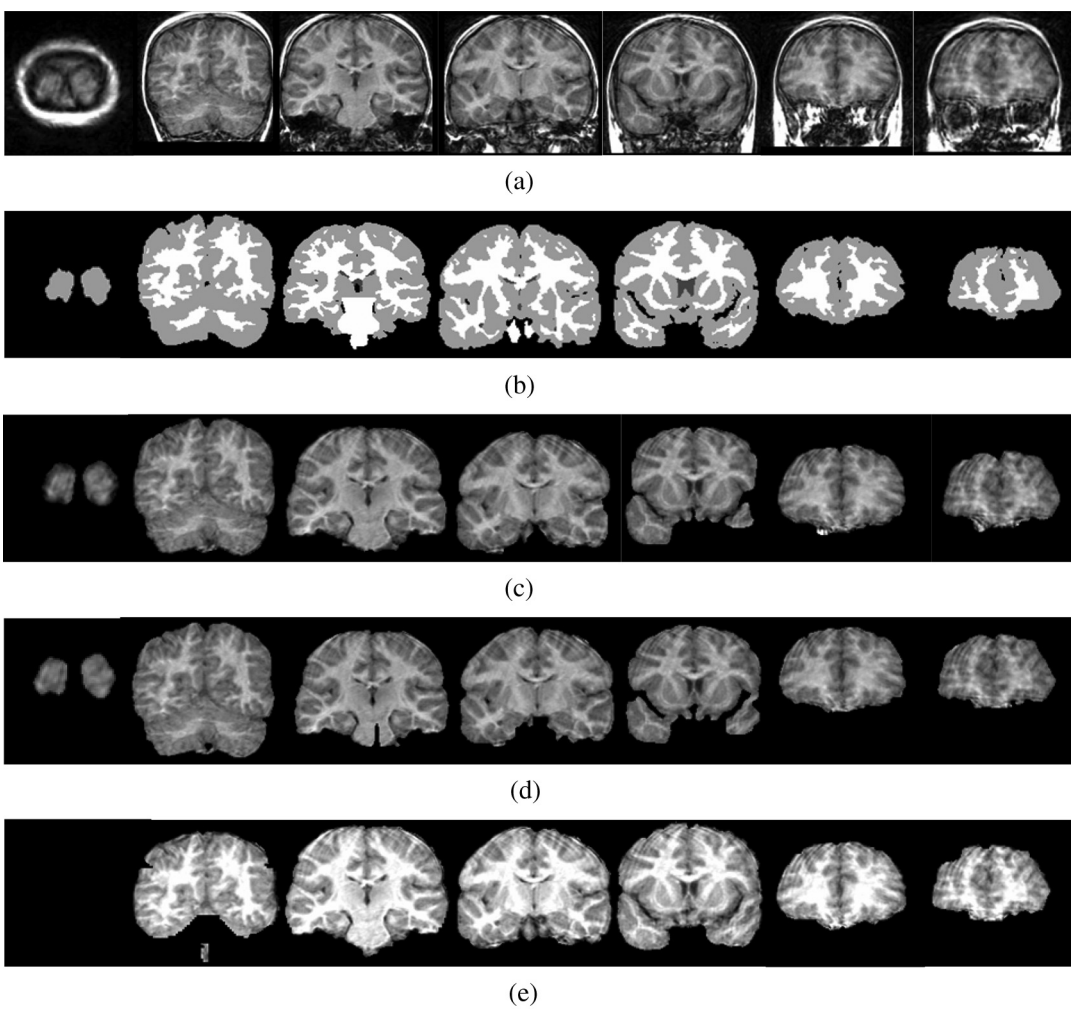

Fig. 10 Images illustrating the segmentation of volume IBSR2_04 through several methods. (a) Brain sections corresponding to the original volume IBSR2_04; (b) manual segmentations provided by the IBSR website; (c) application of Eq. (9) with the parameters defined in Table 3; (d) application of Eq. (12) with the parameters defined in Table 4; and (e) slices obtained from BET using a fractional intensity = 0.5 and vertical gradient = 0.0.

Table 6 Jaccard and Dice indexes corresponding to IBSR2 dataset and segmented with BET, Eqs. (9) and (12) considering the parameters presented in Tables 3 and 4.

	BET		Eq. (12)		Eq. (9)	
Volume	Jaccard	Dice	Jaccard	Dice	Jaccard	Dice
IBSR2_01	0.7802	0.8765	0.9281	0.9627	0.9699	0.9847
IBSR2_02	0.8112	0.8958	0.9516	0.9752	0.9480	0.9733
IBSR2_03	0.8611	0.9254	0.9443	0.9714	0.9603	0.9798
IBSR2_04	0.8336	0.9092	0.9629	0.9811	0.9540	0.9765
IBSR2_05	0.7868	0.8807	0.9252	0.9611	0.9083	0.9519
IBSR2_06	0.7847	0.8794	0.9512	0.9750	0.9233	0.9601
IBSR2_07	0.8113	0.8958	0.8654	0.9278	0.8931	0.9435
IBSR2_08	0.7787	0.8756	0.8402	0.9132	0.8939	0.9440
IBSR2_09	0.8108	0.8955	0.9077	0.9516	0.9164	0.9564
IBSR2_10	0.7099	0.8303	0.8606	0.9251	0.8355	0.9104
IBSR2_11	0.7861	0.8802	0.9191	0.9579	0.9338	0.9658
IBSR2_12	0.7798	0.8763	0.8947	0.9444	0.9441	0.9712
IBSR2_13	0.7912	0.8834	0.9435	0.9709	0.9522	0.9755
IBSR2_14	0.8082	0.8940	0.9634	0.9814	0.9655	0.9824
IBSR2_15	0.8206	0.9014	0.9144	0.9553	0.9511	0.9749
IBSR2_16	0.8385	0.9122	0.9495	0.9741	0.9381	0.9681
IBSR2_17	0.8171	0.8993	0.9268	0.9620	0.9541	0.9765
IBSR2_18	0.8067	0.8930	0.9066	0.9510	0.9066	0.9510

volume. In our case, Eq. (9) takes 16 min and Eq. (12) took 8 min.

ii. BET and the algorithms reported in Refs. 11, 12, and 40 use fewer parameters than Eqs. (9) and (12).

iii. Although the time spent to segment a volume is high compared to the BET, the segmentations obtained with our proposal [Eq. (9)] are better according to the Jaccard and Dice mean indices.

iv. Equation (12) works well; however, the indices presented in Table 7 indicate that Eq. (9) has a better performance.

5 Conclusions

Two morphological transformations were proposed to extract brain in MRIs T1. The first operator [Eq. (9)] presents a better performance than the second one [Eq. (12)] according to the computed Jaccard and Dice mean indices.

Table 7 Jaccard and Dice mean indexes corresponding to IBSR1 and IBSR2 datasets and some reported in the literature.

Method	Jaccard mean	Dice mean
SMHASS (Ref. 11) IBSR1	0.904	0.950
SMHASS (Ref. 11) IBSR2	0.905	0.950
ACNM One (Ref. 12) IBSR1	0.890	0.940
ACNM One (Ref. 12) IBSR2	0.900	0.950
Equation (9) IBSR1	0.935	0.966
Equation (9) IBSR2	0.924	0.963
Equation (12) IBSR1	0.866	0.938
Equation (12) IBSR2	0.919	0.957
BET ISBR1	0.784	0.869
BET ISBR2	0.800	0.899
Method in Ref. 40 using IBSR1	0.923	0.960

Number of slices	Time (s)
5	27.24
10	56.26
20	111.85
40	250.89
60	354.8
80	513.7
160	945

(a)

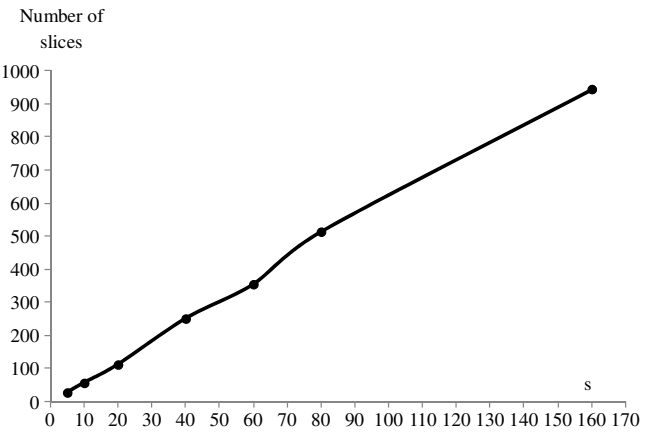

(b)

Fig. 11 Time performance of Eq. (9). (a) Consumed time by Eq. (9) when the number of slices increases. (b) Graph of the information presented in (a).

The idea to segment the brain consisted of smoothly propagating a marker given by the viscous opening into the original volume. For this, adequate parameters must be obtained from a granulometric analysis. The sequential application of such transformations results in a new morphological operator [Eq. (9)] capable of better controlling the reconstruction process. Nevertheless, the new transformation employs several parameters; due to this, a second morphological transformation was obtained from a simplification of the first one [Eq. (12)].

Our proposals were tested using the two brain databases obtained from the IBSR home page. In total, 38 volumes of MR images of the brain were processed. The segmentations were compared through two popular indices with respect to the segmentations obtained from the BET algorithm, with manual segmentations obtained from the IBSR website and with respect to the values of the indices reported in the current literature. When the mean values of the Jaccard and Dice indices are compared, our proposal outperforms the other methodologies. This means that our segmentations are closer to the manual segmentations obtained from the IBSR website. However, the time spent to segment a volume with 160 slices, along with the number of parameters utilized in Eq. (9), is higher compared to the time and the parameters utilized by the BET algorithm.

Although Eq. (12) significantly reduces the number of parameters, Eq. (9) produces better segmentations. In this way, Eq. (12) can be used to get approximated segmentations of the brain.

The main problem of the BET algorithm is that several regions are not detected; the beginning of Fig. 10(e) clearly illustrates this situation. Due to this, the Jaccard and Dice indices fall considerably.

Finally, as future work, the proposal presented in this paper will be improved by the implementation of fast algorithms and/or parallel implementation on graphics processing units using compute unified device architectures technology, so the performance can improve for real-time applications.

Acknowledgments

The author Iván R. Terol-Villalobos would like to thank Diego Rodrigo and Darío T.G. for their great encouragement. This work was funded by the government agency CONACyT México under the Grant 133697.

References

1. A. M. Dale, B. Fischl, and M. I. Sereno, "Cortical surface-based analysis. I. Segmentation and surface reconstruction," *Neuroimage* **9**(2), 179–194 (1999).
2. J. X. Liu, Y. S. Chen, and L. F. Chen, "Accurate and robust extraction of brain regions using a deformable model based on radial basis functions," *J. Neurosci. Methods* **183**(2), 255–266 (2009).
3. S. M. Smith, "Fast robust automated brain extraction," *Hum. Brain Mapp.* **17**(3), 143–155 (2002).
4. H. Hahn and H.-O. Peitgen, "The skull stripping problem in MRI solved by a single 3D watershed transform," *Lect. Notes Comput. Sci.* **1935**, 134–143 (2000).
5. R. Beare et al., "Brain extraction using the watershed transform from markers," *Front. Neuroinf.* **7**(32), 1–15 (2013).
6. B. Dogdas, D. W. Shattuck, and R. M. Leahy, "Segmentation of skull and scalp in 3-D human MRI using mathematical morphology," *Hum. Brain Mapp.* **26**(4), 273–285 (2005).
7. S. Sandor and R. Leahy, "Surface-based labeling of cortical anatomy using a deformable database," *IEEE Trans. Med. Imaging* **16**(1), 41–54 (1997).
8. F. Ségonne et al., "A hybrid approach to the skull stripping problem in MRI," *Neuroimage* **22**(3), 1060–1075 (2004).
9. J. E. Iglesias et al., "Robust brain extraction across datasets and comparison with publicly available methods," *IEEE Trans. Med. Imaging* **30**(9), 1617–1634 (2011).
10. F. Lotte, A. Lecuyer, and B. Arnaldi, "FuRIA: a novel feature extraction algorithm for brain-computer interfaces using inverse models and fuzzy regions of interest," in *3rd Int. IEEE/EMBS Conf. on Neural Engineering, 2007 (CNE '07)*, Kohala Coast, HI, pp. 175–178, IEEE (2007).
11. F. J. Galdames, F. Jaillet, and C. A. Perez, "An accurate skull stripping method based on simplex meshes and histogram analysis for magnetic resonance images," *J. Neurosci. Methods* **206**(2), 103–119 (2012).
12. S. Jiang et al., "Brain extraction from cerebral MRI volume using a hybrid level set based active contour neighborhood model," *Biomed. Eng. Online* **12**(1), 31 (2013).
13. A. Huang et al., "Brain extraction using geodesic active contours," *Proc. SPIE* **6144**, 61444J (2006).
14. S. F. Eskildsen et al., "The Alzheimer's disease neuroimaging initiative, BEaST: brain extraction based on nonlocal segmentation technique," *Neuroimage* **59**(3), 2362–2373 (2012).
15. K. K. Leung et al., "Automated cross-sectional and longitudinal hippocampal volume measurement in mild cognitive impairment and Alzheimer's disease," *Neuroimage* **51**(4), 1345–1359 (2010).
16. K. K. Leung et al., "Alzheimer's disease neuroimaging initiative, brain MAPS: an automated, accurate and robust brain extraction technique using a template library," *Neuroimage* **55**(3), 1091–1108 (2011).
17. P. Dokládal et al., "Topologically controlled segmentation of 3D magnetic resonance images of the head by using morphological operators," *Pattern Recognit.* **36**(10), 2463–2478 (2003).
18. M. A. Balafar et al., "Review of brain MRI image segmentation methods," *Artif. Intell. Rev.* **33**(3), 261–274 (2010).
19. J. C. Bezdek, L. O. Hall, and L. P. Clarke, "Review of MR image segmentation techniques using pattern recognition," *Med. Phys.* **20**(4), 1033–1048 (1993).
20. A. P. Zijdenbos and B. M. Dawant, "Brain segmentation and white matter lesion detection in MR images," *Crit. Rev. Biomed. Eng.* **22**(5–6), 401–465 (1994).
21. L. P. Clarke et al., "MRI segmentation: methods and applications," *J. Magn. Reson. Imaging* **13**(3), 343–368 (1995).
22. C. Fennema-Notestine et al., "Quantitative evaluation of automated skull-stripping methods applied to contemporary and legacy images: effects of diagnosis, bias correction, and slice location," *Hum. Brain Mapp.* **27**(2), 99–113 (2006).
23. D. W. Shattuck et al., "Online resource for validation of brain segmentation methods," *Neuroimage* **45**(2), 431–439 (2009).
24. K. Boesen et al., "Quantitative comparison of four brain extraction algorithms," *Neuroimage* **22**(3), 1255–1261 (2004).
25. B. D. Ward, *Intracranial Segmentation*, Biophysics Research Institute, Medical College of Wisconsin, Milwaukee (1999), AFNI is NIH supported software at http://afni.nimh.nih.gov/pub/dist/doc/program_help/ (23 May 2014).
26. D. W. Shattuck et al., "Magnetic resonance image tissue classification using a partial volume model," *Neuroimage* **13**(5), 856–876 (2001).
27. J. Ashburner and K. J. Friston, "Voxel-based morphometry: the methods," *Neuroimage* **11**(6 Pt 1), 805–821 (2000).
28. V. Popescu et al., "Optimizing parameter choice for FSL-Brain Extraction Tool (BET) on 3D T1 images in multiple sclerosis," *Neuroimage* **61**(4), 1484–1494 (2012).
29. I. Santillán et al., "Morphological connected filtering on viscous lattices," *J. Math. Imaging Vision* **36**(3), 254–269 (2010).
30. J. D. Mendiola-Santibañez et al., "Application of morphological connected openings and levelings on magnetic resonance images of the brain," *Int. J. Imaging Syst. Technol.* **21**(4), 336–348 (2011).
31. Center for Morphometric Analysis, Massachusetts General Hospital, The Internet Brain Segmentation Repository (IBSR) (1995), http://www.cma.mgh.harvard.edu/ibsr/ (23 May 2014).
32. L. Vincent, "Morphological grayscale reconstruction in image analysis: applications and efficient algorithms," *IEEE Trans. Image Process.* **2**(2), 176–201 (1993).
33. F. Meyer and C. Vachier, "Image segmentation based on viscous flooding simulation," in *Mathematical Morphology*, H. Talbot and R. Beare, Eds., pp. 69–77, CSIRO Publishing, Melbourne (2002).
34. C. Vachier and F. Meyer, "The viscous watershed transform," *J. Math. Imaging Vis.* **22**(2–3), 251–267 (2005).
35. P. Maragos and C. Vachier, "A PDE formulation for viscous morphological operators with extensions to intensity-adaptative operators," in *Proc. 15th IEEE Int. Conf. in Image Processing*, San Diego, CA, pp. 2200–2203, IEEE (2008).
36. C. Vachier and F. Meyer, "News from viscous land," in *Proc. of the 8th Int. Symposium on Mathematical Morphology*, , Rio de Janeiro, Brazil, G. J. F. Banon et al., Eds., pp. 189–200, MCT/INPE (2007).
37. L. Vincent, "Fast granulometric methods for the extraction of global image information," in *Proc. 11th Annual Symposium of the South African Pattern Recognition Association*, Johannesburg, South Africa, pp. 119–133, University of Witwatersrand publisher (2000).

38. P. Jaccard, "The distribution of the flora in the alpine zone," *New Phytol.* **11**(2), 37–50 (1912).
39. L. R. Dice, "Measures of the amount of ecologic association between species," *J. Ecol.* **26**(4), 297–302 (1945).
40. H. Zhang et al., "An automated and simple method for brain MR image extraction," *Biomed. Eng. Online* **10**(1), 81 (2011).
41. H. Heijmans, *Morphological Image Operators*, Academic Press, Boston, Massachusetts (1994).
42. J. Serra and P. Salembier, "Connected operator and pyramids," *Proc. SPIE* **2030**, 65–76 (1993).
43. C. Rorden and M. Brett, "Stereotaxic display of brain lesions," *Behav. Neurol.* **12**(4), 191–200 (2000).

Jorge Domingo Mendiola-Santibañez received his PhD degree from the Universidad Autónoma de Querétaro (UAQ), México. Currently, he is a professor/researcher at the Universidad Autónoma de Querétaro. His research interests include morphological image processing and computer vision.

Martín Gallegos-Duarte is an MD and a PhD student at the Universidad Autonoma de Querétaro. He is head of the Strabismus Service at the Institute for the Attention of Congenital Diseases and Ophthalmology-Pediatric Service in the Mexican Institute of Ophthalmology in the state of Queretaro, Mexico.

Miguel Octavio Arias-Estrada is a researcher in computer science at National Institute of Astrophysics, Optics and Electronics, Puebla, Mexico, with a PhD degree in electrical engineering (computer vision) from Laval University (Canada) and BEng and MEng degrees in electronic engineering from University of Guanajuato (Mexico). Currently, he is a researcher at INAOE (Puebla, México). His interests are computer vision, FPGA and GPU algorithm acceleration for three-dimensional machine vision.

Israel Marcos Santillán-Méndez received the BS degree in engineering from the Instituto Tecnológico de Estudios Superiores de Monterrey and his MS degree and PhD degree in engineering from Facultad de Ingeniería de la Universidad Autónoma de Querétaro (México). His research interests include models of biological sensory and perceptual systems and mathematical morphology.

Juvenal Rodríguez-Reséndiz received his MS degree in automation control from University of Querétaro and PhD degree at the same institution. Since 2004, he has been part of the Mechatronics Department at the UAQ. He is the head of the Automation Department. His research interest includes signal processing and motion control. He serves as vice president of IEEE in Queretaro State.

Iván Ramón Terol-Villalobos received his BSc degree from Instituto Politécnico Nacional (I.P.N. México), his MSc degree from Centro de Investigación y Estudios Avanzados del I.P.N. (México). He received his PhD degree from the Centre de Morphologie Mathématique, Ecole des Mines de Paris (France). Currently, he is a researcher at CIDETEQ (Querétaro, México). His main current research interests include morphological image processing, morphological probabilistic models, and computer vision.